Journal of the Korean Physical Society
https://doi.org/10.1007/s40042-024-01205-5

Online ISSN 1976-8524
Print ISSN 0374-4884

ORIGINAL PAPER - ATOMS, MOLECULES AND OPTICS

Development of the collinear laser spectroscopy (CLaSsy) at RAON

Sung Jong Park[1] · Seong Gi Jo[1] · Chaeyoung Lim[2] · Kyoungho Tshoo[1] · Cheolmin Ham[1] · Dong Geon Kim[1] · Donghyun Kwak[1] · Seong Jae Pyeun[1] · Taeksu Shin[1] · Jung Bog Kim[3] · Jens Lassen[4]

Received: 29 July 2024 / Revised: 2 October 2024 / Accepted: 7 October 2024

Abstract
Collinear laser spectroscopy (CLS) has been used as a tool for nuclear physics that provides fast, sensitive, and accurate means for the determination of nuclear ground-state properties via optical isotope shift and hyperfine structure measurements. The model-independent extraction of nuclear ground-state properties from optical spectra delivers important physics results to test the predictive power of nuclear models. A CLS system (called CLaSsy) has been installed in RAON's ISOL beamline and developed for the study of basic nuclear properties, such as nuclear spins, magnetic dipole moments, electric quadrupole moments, and mean-square charge radii. The neutralization efficiency of the vertical charge-exchange cell on the CLS beamline has been tested using the stable Ar ion beams produced from an off-line ion source. This off-line experiment will open new opportunities for laser spectroscopy measurement of atomic state of unstable isotopes produced at the ISOL facility at the Institute for Rare Isotope Science in Korea.

Keywords Collinear laser spectroscopy · Nuclear properties · Hyperfine structure · Isotope shifts

1 Introduction

In recent decades, laser spectroscopy techniques have made significant contributions in our understanding of exotic nuclei in radioactive ion beam (RIB) facilities worldwide [1–3]. This is achieved through determining multiple fundamental properties of nuclear ground and isomeric states, such as nuclear spins I, magnetic dipole μ and electric quadrupole moments Q, and mean-square nuclear charge radii $\langle r^2 \rangle$, via the measurement of hyperfine structures and isotope shifts in the atomic or ionic spectra of the nuclei of interest.

Online laser spectroscopy experiments at RIB facilities also stimulated the development of collinear laser spectroscopy (CLS), which was validated as an approach at TRIGA, Mainz [4, 5], achieving both a high resolution and sensitivity for the time. Soon after, the CLS method was applied at online facilities and used extensively in the study of nuclear properties of unstable isotopes [6, 7]. Such studies have been carried out at RIB facilities based on the Isotope Separation OnLine (ISOL) technique, such as ISOLDE-CERN [8, 9], IGISOL of JYFL [10], and ISAC of TRIUMF [11], where the RIBs are delivered at a suitable energy (e.g., ~ 30–60 keV). Until now, the majority of laser spectroscopy experiments of unstable isotopes have been performed at ISOL-type RIB facilities, such as ISOLDE-CERN. These facilities directly produce low-energy RIBs with favorable properties for laser spectroscopy experiments. The development of new-generation facilities, such as the recently operational FRIB in the US [12], as well as those still under construction like SPIRAL2-GANIL in France [13], FAIR in Germany [14], HIAF in China [15], and RAON in South Korea [16], will allow unprecedented access to short-lived isotopes. Due to their recognized potential to make meaningful contributions across multiple fields of science in addition to the study of exotic nuclei, online laser spectroscopy setups are either already in operation or planned at nearly every current and upcoming RIB facility around the world and are shown in Fig. 1.

✉ Sung Jong Park
sjpark@ibs.re.kr

[1] Institute for Rare Isotope Science, Institute for Basic Science (IBS), Daejeon 34000, Korea

[2] Department of Accelerator Science, Korea University Sejong Campus, Sejong 30015, Korea

[3] Department of Physics Education, National University of Education, Cheongju 28173, Korea

[4] TRIUMF, 4004 Wesbrook Mall, Vancouver, BC V6T 2A3, Canada

Published online: 24 October 2024

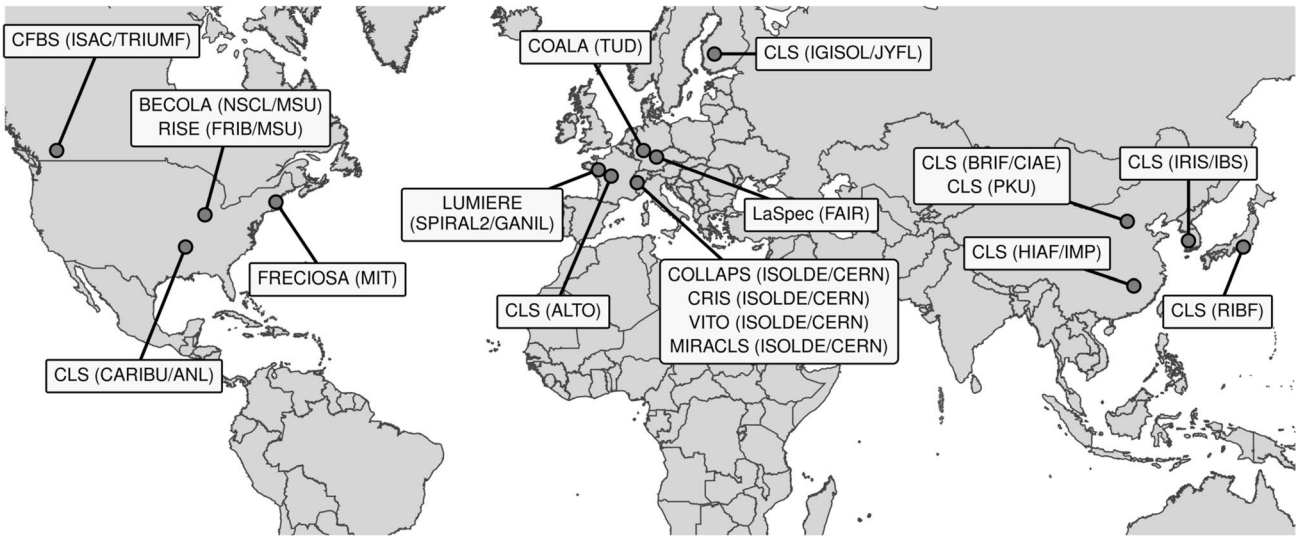

Fig. 1 Distribution of collinear laser spectroscopy setups at the different radioactive ion beam facilities around the world

CLS experiments rely on the measurement of Doppler-free optical spectra by overlapping a low-energy (a few tens of keV) atom or ion beam with a high-resolution laser beam. In this geometry, the accelerated ionic ensembles experience a velocity compression along the axis of their motion. The compression arises from an acceleration to well-defined energy E preserving an original energy spread δE but reducing the corresponding velocity spread to

$$\delta v = \frac{1}{\sqrt{2mE}}\delta E. \tag{1}$$

This compression reduces the Doppler broadening of the spectral lines allowing high-precision laser spectroscopy of short-lived isotopes. In the case of work with fast atomic beams, where an alkali metal vapor cell is used to neutralize ions to fast atoms, tuning the potential of the vapor cell achieves the final velocity tuning.

In this report, we describe the ongoing development of a CLS setup in the Institute for Rare Isotope Science (IRIS). The CLS beamline has been installed with an existing ISOL system and was tested using an off-line ion source by measuring neutralization efficiency of Ar ion beams.

2 Atomic structure and laser nuclear spectroscopy

Laser spectroscopy techniques are powerful tools that can simultaneously access multiple fundamental properties of atomic nuclei (spins, electromagnetic moments, and charge radii) in a nuclear model-independent way. Measurement of these quantities is realized by probing the hyperfine structure and isotope shift of atomic/ionic energy levels.

2.1 Hyperfine structure

The hyperfine interaction energy of a state with hyperfine quantum number F, total angular momentum quantum number J, and nuclear spin I is given by

$$\Delta E_{\mathrm{HFS}} = \frac{AK}{2} + B\frac{\frac{3}{2}K(K+1) - 2I(I+1)J(J+1)}{4I(2I-1)J(2J-1)}. \tag{2}$$

Here, $K = F(F+1) - I(I+1) - J(J+1)$, $A = g\mu_N B(0)\hbar/\boldsymbol{I}\cdot\boldsymbol{J}$ and $B = eQ_s\phi_{jj}(0)$ are hyperfine constants, $\mu_N(Q_s)$ are the Bohr magneton (electric quadrupole) moment of the nucleus, $B(0)$ is the magnetic field generated at the nuclear site by electrons, and $\phi_{jj}(0)$ is the electric field gradient produced by electrons at the nucleus. The dependence of the hyperfine splitting on nuclear spin I ensures that, given enough splittings exist, a unique assignment of the nuclear spin can be made.

2.2 Isotope shift

The frequency of the same atomic transition is observed to shift between different isotopes of the same element. For nuclei with atomic masses A and A', the frequency shift, known as the isotope shift, is generally defined as

$$\delta\nu^{A,A'} = \nu^{A'} - \nu^{A}, \tag{3}$$

where ν^A is the frequency of the atomic transition for isotope A. In general, this can be approximated as being composed

of two independent components, the mass shift arising from the change in total mass of the system, and the field shift arising from the change in the spatial distribution of the nuclear charge. The mass shift is an effect of atomic kinetic energy change to the electronic energy structure and the field shift appears due to the effect of finite extension of the nuclear charge distribution on the electronic binding energy. The field shift provides an estimate of the change of nuclear charge radius within an isotopic series or between isomers. The ratio of field shifts and difference of mass shift factors can be obtained separately through King Plot.

3 Experiment

3.1 Collinear laser spectroscopy beamline

A schematic diagram of the CLS setup is shown in Fig. 2. The CLS beamline is connected to the existing ISOL beamline via RI beamline, which comprises beam guiding optics and ion beam diagnostic elements (not shown). An off-line ion source (OLIS) is connected through SI beamline to test the beamline using stable isotopes. The CLS beamline was made at TRIUMF in Canada, and thus, this beamline can be used to provide nuclear spin-polarized ion beams [11]. For this possible application, an additional bender (B2) is installed downstream of the CLS beamline on which an application beamline (App. beamline) will be connected in the future.

In the first stage, the ^{40}Ar ions are produced in a commercial off-line ion source (SO-55, High Voltage Engineering Europa B.V.), extracted, and refocused with an einzel lens. The argon-ion beam is accelerated to an energy of 20 keV using a high-voltage power supply (HCP 35, FuG Elektronik GmbH) with a specified relative voltage stability of better than 10^{-5} over 8 h. The extracted ions are then further corrected by a group of horizontal and vertical steerers (orange boxes) and a set of quadrupoles (red boxes) before the beams are directed into the CLS beamline by a pair of 45° electrostatic bender (B1). The SI beamline includes a Faraday cup (S-F1) located before the bender to measure the ion current from the source.

As show in Fig. 2, the CLS beamline is installed downstream of the SI beamline. The incoming continuous ion beam for the OLIS is guided to the CLS beamline by the electrostatic bender (B1). Downstream of the bender plates in the deflection chamber, a pair of electrostatic plates follows to correct the ion beam direction. The ion beam is then transported through the CLS beamline using two sets of quadrupole doublets with *x*–*y* steerer plates. The guided ion beam is then transported to a specially designed electrode arrangement (referred to as *post-accelerator*) to modify the kinetic energy of the incoming ion beam by controlling the voltage of up to ±10 keV. After the voltage-scanning electrode, the ion beam is injected into the charge-exchange cell (CEC), where the ions are neutralized via collision with alkali vapor. The CEC is followed by a chamber (VC10) housing a photomultiplier tube positioned perpendicularly to the beam axis, which can be used to detect fluorescence

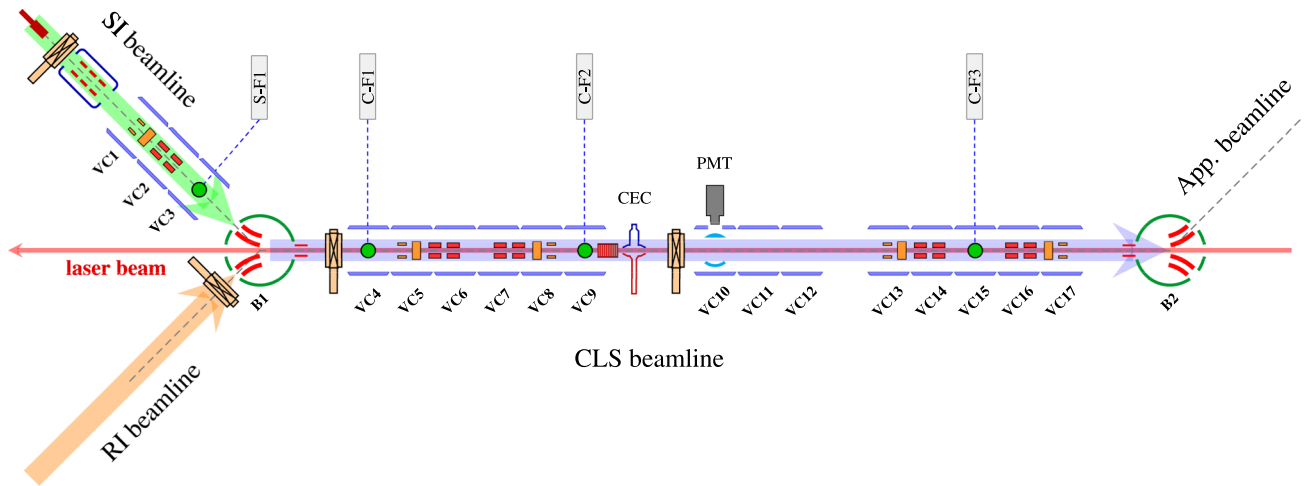

Fig. 2 A schematic drawing of the CLS beamline. Stable (unstable) isotopes are transported to the 45° Y-bender (B1) along the SI beamline (RI beamline). The ion beam deflected at the bender B1 is overlapped with counter-propagating laser beam (red arrow) on the CLS beamline. The ion beam is neutralized in the charge-exchange cell (CEC). A fluorescence detection system for the laser spectroscopy is installed at the chamber VC10, where the resulting fluorescence is collected using mirror and lens systems and detected with a photomultiplier tube (PMT). See text for more details

light emitted by the excited ions or atoms. The photomultiplier tubes in this detection area are used for determining the resonant laser frequency through optical detection of the fluorescence decay from an isotope of interest. At the end of the CLS beamline, a series of ion-optics elements and an electrostatic bender (B2) are installed for the possible future experiments. For this, an extended beamline where the optical pumping takes place will be installed between the chambers VC12 and VC13 in the future.

3.2 Beam diagnostics and ion optics

For the diagnostics purposes, three Faraday cups (C-F1, C-F2, and C-F3) with a wire scanner are introduced along the CLS beamline to record ion beam current and beam profile. Here, C-F1 is used to measure the beam current ($I_{\text{C- F1}}$) after the 45° bender. The C-F2 and C-F3 measure the ion beam currents ($I_{\text{C- F2}}$ and $I_{\text{C- F2}}$) before and after the CEC, respectively. The typical argon-ion beam intensity before and after the CEC was 1–2 μA, measured with a Faraday cups including a secondary-electron suppressor (C-F2 and C-F3). The wire scanners are used to observe the beam profile, which helps in the optimization of the beam transmission by tuning the beam optics elements.

Ion-optical beam transmission simulations were performed to benchmark the effect that the deflector and ion-optics components have on the path of the beam and the transmission that can be expected. The beam optics of the present setup is simulated using the computer code COSY and SIMION (Fig. 3). The 16-mm openings of the CEC determine the acceptance of the incident ion beam, and the preliminary beamline simulations showed a good transmission through the entire line from the OLIS to the Faraday cup (C-F3).

3.3 Charge exchange cell (CEC)

Spectroscopy of neutral atom beams is often advantageous, since the wavelengths of atomic transitions are usually easier to detect than those of the corresponding ion. A charge-exchange cell (CEC) is used to produce the fast atom beams from the incident ion beams. A CEC is placed immediately in front of the optical detection region in the CLS beamline, and an alkali vapor is generated inside the CEC by heating a solid alkali. The ion beam is passed through the alkali vapor and neutralized through ion-atom charge-exchange reactions.

A CEC with vertical configuration used in this work was designed and has been in operation for the last several years at the TRIUMF Laboratory in Canada. The performance characteristics of the vertical CEC were determined

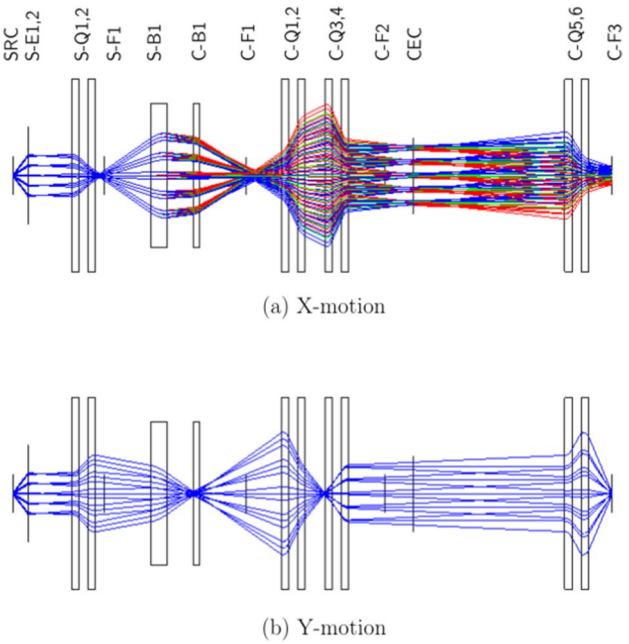

Fig. 3 The ion-optics calculation for the entire line from the OLIS (SRC) to the Faraday cup (C-F3) via optics components including einzel lens (E), electrostatic bender (B), and quadrupoles (Q)

by neutralizing a 20-keV argon-ion beam. Another type of CEC called the horizontal CEC was developed and constructed at the University of Mainz in Germany, and the performance characteristics of two CECs were determined by neutralizing a 10-keV rubidium-ion beam in a potassium vapor, resulting in the similar behavior in terms of neutralization efficiency for both CECs [17].

Figure 4 depicts the details of CEC components. Four thermocouples are mounted to monitor the temperature at different positions of the CEC. The temperature of the reservoir ($T1$) can be up to 300 °C for Rb to produce a sufficiently dense vapor for charge exchange. To minimize diffusion of the Rb vapor into the rest of the beamline, the ends of the CEC on the beamline are kept at a lower temperature of about 55 °C, above the melting point of Rb (38.9 ℃). The lower temperature condenses the vapor into a liquid which flows back to the reservoir. This minimizes the loss of vapor to the rest of the beamline and ensures a high vapor density along the vertical axis of the CEC.

The reservoir is connected to an interaction region by a stainless-steel vertical tube of 22 mm inner diameter. The effective interaction length, however, is mostly determined from the solid angle of the beam axis seen from alkali in the reservoir and is estimated to be 35 mm. Along the beamline, the CEC has two openings with a diameter of 16 mm on both sides, which determine the acceptance of the incident ion beam.

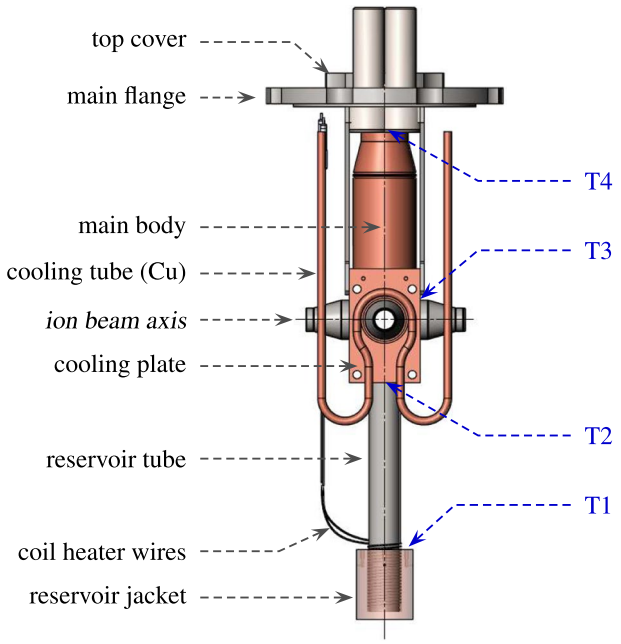

Fig. 4 The charge-exchange cell is shown with the thermocouples to monitor the temperature at different positions of the CEC ($T1$–$T4$)

4 Results and discussion

The fraction $\eta = (1 - I/I_0)$ is the neutralization efficiency of the CEC. I_0 is defined as $I_0 = I_{\text{C- F3}}/I_{\text{C- F2}}$ when CEC is off and $I = I_{\text{C- F3}}/I_{\text{C- F2}}$ when CEC is on. The corresponding $I_{\text{C–F3}}$ is normalized with respect to I_{C-F2} to take care of fluctuations in $I_{\text{C–F2}}$ due to any reason other than charge-exchange mechanism. In this way, the attenuation in $I_{\text{C–F3}}$ can be made sure to be happening only due to the charge-exchange process.

The neutralization efficiency of the argon-ion beam was calculated using an attenuation model of a particle beam moving through a medium [17]

$$\eta \equiv (1 - \exp^{-n\sigma l}) \times 100\%, \tag{4}$$

where n is the alkali vapor density in cm^{-3}, σ is the cross-section of the neutralization process in cm^2, and l is the effective interaction length in cm.

The vapor density n can be modeled as

$$n = \frac{10^{A/T+B} N_{\text{A}}}{V_{\text{mol}} p_0}, \tag{5}$$

assuming the vapor pressure is saturated for a given temperature. Here, T is the temperature of the alkali vapor in kelvin, N_{A} is Avogadro's number, V_{mol} is the standard molar volume, and p_0 is the standard pressure. Typical values of A and B for rubidium are −4040 K and 4.312, respectively.

Figure 5a shows the neutralization efficiency of the rubidium-ion beam as a function of the temperature of the potassium vapor for the horizontal (black) and vertical (blue) CECs calculated by Eq. (4), where the values of A and B for potassium are −4453 K and 4.402, respectively [17]. From this reference plot, for the vertical CEC with the rubidium vapor, one can expect the neutralization curve (red), as shown in Fig. 5b and c.

The measured neutralization efficiency is shown in Fig. 5c as a function of reservoir temperatures of the CEC. The cross-section for the charge-exchange reaction was

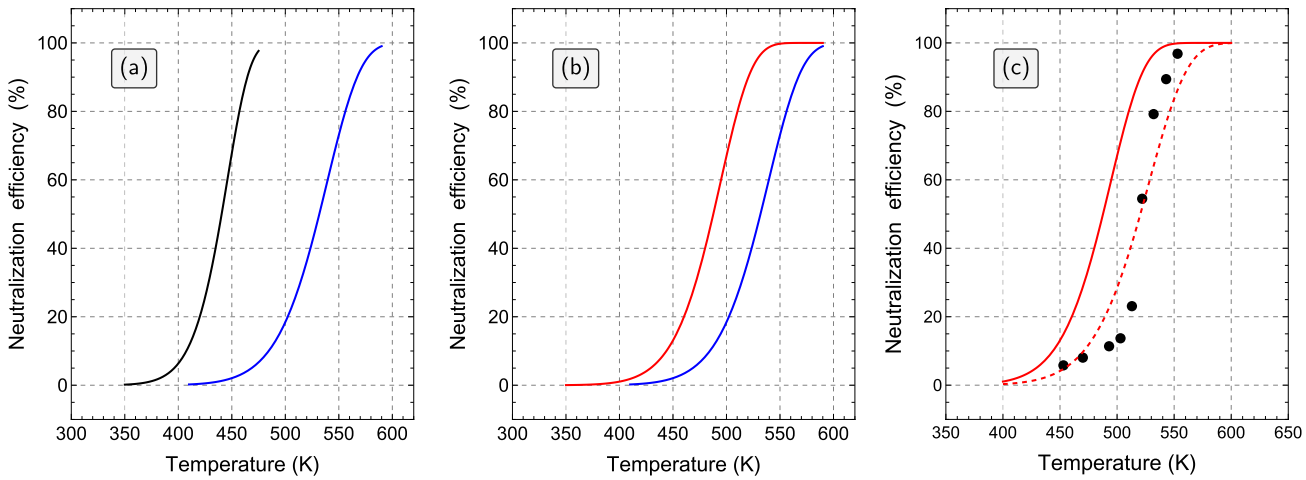

Fig. 5 Neutralization efficiency curves. **a** The neutralization efficiency of the rubidium-ion beam as a function of the temperature of the potassium vapor for the horizontal (black) and vertical (blue) CECs calculated by Eq. (4) [17]. **b** The calculated neutralization efficiency of the argon-ion beam as a function of the temperature of the potassium (blue) and the rubidium (red) vapors for the vertical CEC. **c** The experimental results of the neutralization efficiency of the argon-ion beam for the vertical CEC (dotted line) and the fitted curve (dashed line) to obtain the cross-section (σ), which were compared with the calculation result [red solid line as in **b**]

deduced from a fit of Eq. (4) to the data shown in Fig. 5c, and $\sigma = 2.1 \times 10^{-17}$ cm^2 was obtained. The cross-section obtained in this work using rubidium vapor is smaller than that of the same vertical CEC using potassium vapor [17].

A linear variation of the neutralization efficiency 10–90% was obtained for the neutralization curve. The slope indicates that the factor $n \times l$ behaved similarly as a function of the reservoir temperature. The slope of the neutralization efficiency from the experimental data is higher than the expected value from Eq. (4). This increase is attributed to the temperature distribution of the rubidium vapor jet in the interaction region and the rubidium vapor pressure well below the saturated vapor pressure.

5 Summary and outlook

In summary, a collinear laser spectroscopy setup at RAON has been developed on the basis of the collinear fast beam laser spectroscopy setup at TRIUMF [18]. To evaluate the general performance of the CLS beamline, the CEC was tested using argon beam of 20-keV energy produced using an off-line ion source (OLIS). This performance test of the CEC demonstrates the overall performance of the present CLS setup including the operation of the OLIS, the vacuum system of the beamline, the beam diagnostics, and the ion beam transmission. The stable argon beam from the OLIS was first neutralized in the Rb cell.

This successful operation of the CLS setup has opened new opportunities for laser spectroscopy measurement of unstable isotopes at the ISOL facility at RAON in Korea. A resonance ionization laser ion source (RILIS) has been developed at RAON for the generation of pure beams of short-lived nuclei for experimental nuclear research [19]. In the commission phase, the RILIS is being improved and used to produce RI beams, e.g., Al and Mg isotopes using a SiC target with a 70 MeV proton beam, which will be used to evaluate the collinear laser spectroscopy and the mass measurement system at RAON ISOL facility [20]. The present CLS setup would be further upgraded as a nuclear spin polarizer using optical pumping technique [21] as used at ISOLDE [22, 23] and TRIUMF [18] to study the nuclear properties of exotic isotopes.

Acknowledgements This work was supported by the Institute for Basic Science (IBS-I001-D1) and by the National Research Foundation of Korea (NRF) funded by Ministry of Science and ICT (RS-2022-00165168). J.B. Kim is grateful for the support of the National Research Foundation of Korea (NRF-2021R1F1A1060385).

References

1. P. Campbell, I.D. Moore, M.R. Pearson, Prog. Part. Nucl. Phys. **86**, 127 (2016)
2. X..F. Yang, S..J. Wanga, S..G. Wilkins, R..F. Garcia Ruiz, Prog. Part. Nucl. Phys. **129**, 104005 (2023)
3. H.-J. Kluge, W. Nörtershäuser, Spectrochim. Acta Part B **58**, 1031 (2003)
4. K.-R. Anton, S.L. Kaufman, W. Klempt, G. Moruzzi, R. Neugart, E.-W. Otten, B. Schinzler, Phys. Rev. Lett. **40**, 642 (1978)
5. B. Schinzler, W. Klempt, S. Kaufman, H. Lochmann, G. Moruzzi, R. Neugart, E.-W. Otten, J. Bonn, L. Von Reisky, K. Spath, J. Steinacher, D. Weskott, Phys. Lett. **79B**, 209 (1978)
6. R. Neugart, Nucl. Instrum. Methods Phys. Res. **186**, 165 (1981)
7. A.C. Mueller, F. Buchinger, W. Klempt, E.W. Otten, R. Neugart, C. Ekström, J. Heinemeier, Nuclear. Phys. A **403**, 234 (1983)
8. M.J.G. Borge, B. Jonson, J. Phys. G Nucl. Part. Phys. **44**, 044011 (2017)
9. W. Nöstershäuser, Hyperfine Interact. **198**, 73 (2010)
10. I.D. Moore, P. Dendooven, J. Ärje, Hyperfine Interact. **223**, 15 (2012)
11. A. Voss, T.J. Procter, O. Shelbaya, P. Amaudruz, F. Buchinger, J.E. Crawford, S. Daviel, E. Mané, M.R. Pearson, W..Al. Tamimi, Nucl. Inst. Methods Phys. Res. A **811**, 57 (2016)
12. T. Glasmacher, B. Sherrill, W. Nazarewicz, A. Gade, P. Mantica, J. Wei, G. Bollen, B. Bull, Nucl. Phys. News **27**, 28 (2017)
13. S. Gales, Prog. Part. Nucl. Phys. **59**, 22 (2007)
14. J. Eschke, J. Phys. G Nucl. Part. Phys. **31**, S967 (2005)
15. Y. Yang, L.T. Sun, Y.H. Zhai, Y.J. Zhai, Z. Shen, C. Qian, W.P. Dou, W. Ma, L. Lu, Y.H. Guo, X. Fang, Y.J. Yuan, L.P. Sun, J.C. Yang, H.W. Zhao, Phys. Rev. Accel. Beams **22**, 110101 (2019)
16. Y.J. Kim, Nucl. Instrum. Methods Phys. Res. B **463**, 408 (2020)
17. A. Klose, K. Minamisono, Ch. Geppert, N. Frömmgen, M. Hammen, J. Krämer, A. Krieger, C.D.P. Levy, P.F. Mantica, W. Nörtershäuser, S. Vinnikova, Nucl. Inst. Methods Phys. Res. A **678**, 114 (2012)
18. R. Li, J. Lassen, C.D.P. Levy, M. Roman, A. Teigelhöfer, V. Karner, G.D. Morris, M. Stachura, A. Gottberg, Nucl. Inst. Methods Phys. Res. B **541**, 228 (2023)
19. S.J. Park, J.B. Kim, Hyperfine Interact. **241**, 39 (2020)
20. J. Lee, H.J. Yim, T. Hashimoto, Y Ho. Park, W. Hwang, S.J. Park, J.W. Jeong, S. Heo, K.H. Yoo, Y.H. Yeon, D.J. Park, J. Kim, B.H. Kang, J.Y. Moon, T. Shin, Nucl. Instrum. Methods Phys. Res. B **524**, 17 (2023)
21. S.J. Park, T. Shin, J.H. Lee, G.D. Kim, Y.K. Kim, J. Opt. Soc. Am. B **31**, 2278 (2014)
22. M. Kowalska, P. Aschenbrenner, M. Baranowski, M.L. Bissell, W. Gins, R.D. Harding, H. Heylen, G. Neyens, S. Pallada, N. Severijns, Ph. Velten, M. Walczak, F. Wienholtz, Z.Y. Xu, X.F. Yang, D. Zakoucky, J. Phys. G Nucl. Part. Phys. **44**, 084005 (2017)
23. W. Gins, R.D. Harding, M. Baranowski, M.L. Bissell, R.F. Garcia Ruiz, M. Kowalska, G. Neyens, S. Pallada, N. Severijns, Ph. Velten, F. Wienholtz, Z.Y. Xu, X.F. Yang, D. Zakoucky, Nucl. Instrum. Methods Phys. Res. A **925**, 24 (2019)